CrystEngComm

Accepted Manuscript

ROYAL SOCIETY OF CHEMISTRY

www.rsc.org/crystengcomm

Synthesis and formation mechanism of morphology-controllable indium containing precursors and optical properties of the derived In_2O_3 particles

Zhijie Lin[a], Qi Zhu[a], Yu Dong[a], Shaohong Liu[a,b], Ji-Guang Li[c*], Xiaodong Li[a], Di Huo[a], Mu Zhang[a], Ming Xie[b], Xudong Sun[a]*

[a] Key Laboratory for Anisotropy and Texture of Materials (Ministry of Education), School of Materials Science and Engineering, Northeastern University, Shenyang, Liaoning 110819, China

[b] State Key Laboratory of Advanced Technologies for Comprehensive Utilization of Platinum Metals, Kunming Institute of Precious Metals, Kunming, 650106, China

[c] Advanced Materials Processing Unit, National Institute for Materials Science, 1-2-1 Sengen, Tsukuba, Ibaraki 305-0044, Japan

* Corresponding author:

Prof. Xudong Sun

Tel: +86-24-83691566

Fax: +86-24-23906316

Email: xdsun@mail.neu.edu.cn

Prof. Ji-Guang Li

Email: LI.Jiguang@nims.go.jp

Abstract

In_2O_3 particles with three distinctive morphologies of 1D rods, 2D disks and 3D cubes were converted from their respective precursors synthesized by a facile urea-based homogeneous precipitation method. Two kinds of precursor phases, including $In(OH)_3$ and $InOHSO_4(H_2O)_2$, were obtained. In the case of high urea concentration, mesocrystalline rod-like $In(OH)_3$ particles were produced by oriented primary particle aggregation induced by the urea coordination on {012} of the primary particles. In contrast, cube-like $In(OH)_3$ was obtained by Ostwald ripening in low concentration urea solution. The addition of K_2SO_4 facilitates the formation of In-sulfate complex, and $InOHSO_4(H_2O)_2$ precursor disks about 2 μm in diameter were formed. It is suggested that the urea absorbed on the active growth sites of the precursor leads to the formation of round disks instead of hexagonal plates. Upon blue light excitation, the three types of In_2O_3 particles obtained from their respective precursors exhibited a morphology-dependent photoluminescence behavior (disks > cubes > rods), but did not differ much in the positions of the PLE and PL bands of the luminescence. The emissions (in the range 500~540 nm) from In_2O_3 are associated with the oxygen vacancy, and highly dependent on the annealing atmosphere.

1. Introduction

In recent years, inorganic particles with regular morphologies have attracted considerable attentions due to their size/shape-dependent properties and potential application. Owing to its special wide-gap transparent semiconducting and optical properties, indium oxide has been widely applied to microelectronic devices such as solar cells, flat-panel displays, sensors and so on[1-5]. In earlier literature, In_2O_3 and its precursors were mostly prepared by the high temperature vapor phase reaction[6-9] and wet chemical methods[5,10-16]. Using these techniques, an increasing number of morphologies have been reported. For example, Yadav and coworkers proposed a chemical vapor deposition method and obtained nanorods of In_2O_3.[9] Mu et al. reported a mild sol-gel technique using citrate acid and prepared indium oxide octahedrons loaded on glass substrates.[11] Jadhav and coworkers developed a hydrothermal method and fabricated cubes and maize-corns of $In(OH)_3$.[13] Liu and coworkers proposed a simple mixed solvothermal process and synthesized 18-facet $In(OH)_3$ polyhedra.[15-16] Although profitable results have been achieved in recent years, some drawbacks, such as high-cost equipment or organic surfactants, low yield, long reaction time, and high environment loads have severely limited practical applications of In_2O_3. A facile and cheap method is still desired.

Urea-based homogeneous precipitation has been an important method for synthesizing precipitates with regular microstructures from metal ions in aqueous solution.[14,17-19] The mild decomposition of urea provides slow and uniform production of anionic species into the system.[20] It has the advantage of avoiding localized

distribution of the reactants, making it possible to exercise control over nucleation and particle growth, which is important for understanding the basic crystal growth mechanism.

It is widely known that bulk In_2O_3 cannot emit light at room temperatures.[21] However, earlier reports indicate that In_2O_3 with peculiar morphology can emit visible and ultraviolet light, such as yellow-emission at 580 nm for In_2O_3 nanotowers under 325 nm excitation,[22] red emission for In_2O_3 nanowires using a He-Cd laser (325 nm) as the excitation source,[23] the emission at 410 and 460 nm for In_2O_3 films under 350 nm excitation[24] and broad emission at 420 nm and 470 nm with a shoulder at 450 nm under an Ne laser excitation at 280 nm.[25] The emission was attributed to the near band edge emission or the defect-induced emission.[21-25] It is believed that the photoluminescence performance of In_2O_3 powders is highly dependent on morphologies and preparation technics. Most of the earlier works focused on the luminescence excited by UV light. Usually, the optical band gap (3.7 eV) in bulk In_2O_3 is higher than the fundamental band gap (2.7 eV), since the direct optical transition from valence band maximum to the conduction band minimum is forbidden.[26] It was reported that the optical band gap in nanostructured In_2O_3 can be as low as 2.7 eV by removing the prohibition of electronic transitions.[27] Thus, nanostructured In_2O_3 should have the ability to be excited by blue light. Considering the harm from UV light to packaging materials and illuminated objects, blue light excited luminescence behavior of In_2O_3 is favorable for practical applications.

In this work, three typical indium-complex precursors were synthesized by a

urea-based homogeneous precipitation technique. In_2O_3 particles with three regular morphologies, 1D rods, 2D disks and 3D cubes, were obtained by calcining their respective precursors. The underlying mechanisms for the nucleation and growth of the precursors were discussed systematically. Photoluminescence behavior of the as-prepared In_2O_3 upon 444 nm (blue light) excitation was investigated. The effect of morphologies and annealing treatment on the PL emission was discussed.

2. Experimental

The starting materials, including indium trichloride ($InCl_3 \cdot 4H_2O$), urea (CH_4N_2O) and potassium sulfate (K_2SO_4), are all of analytical purity. All of them were purchased from Sinopharm Chemical Reagent Co., Ltd and used as received without further purification. In a typical synthesis, 0.5 mol/L $InCl_3$ aqueous solution was prepared, and proper amounts of urea and K_2SO_4 were added under magnetic stirring. Then, the solution was heated to a certain temperature for a certain time. After washing and drying, the samples were used for further analysis. The conditions for synthesizing the precursors are listed in Table 1. The final products were obtained through a heat treatment for 1 h in air at 600 ^oC for samples S1 and S2, and 900 ^oC for S3. Some obtained powder products were annealed in a tube furnace with program-controlled temperature and different atmospheres.

Table 1. The experimental parameters for In_2O_3 precursor synthesis.

Sample	Concentration of urea (mol/L)	Reaction temperature (^oC)	Reaction time (hour)	Concentration of K_2SO_4 (mol/L)	Morphology

S1	9	90	2	0	rods
S2	0.06	90	5	0	cubes
S3	9	90	1	9	disks

The morphologies of the three typical In_2O_3 samples and the corresponding precursors were observed via field emission scanning electron microscopy (FE-SEM, Ultra Plus, Carl Zeiss AG, Germany) and transmission electron microscopy (TEM, Tecnai G20, FEI, USA) with selected area electron diffraction (SAED) for detailing structures. Phase identification was performed by X-ray diffraction (XRD, Model PW 3040/60, PANALYTICAL B.V, Netherlands). Fourier transform infrared spectroscopy (FT-IR) was performed by the standard KBr method (Spectrum RXI, Perkin-Elmer, USA). Differential thermal analysis - thermo gravimetric (DTA/TG) analysis (Model SETSYS Evolution-16, SETARAM, France) of the precursor was made under flowing oxygen with a heating rate of 10 ^{o}C/ min. BET analysis was performed via nitrogen adsorption at 77K (Model Tri-Star II 3020, Micrometritics, USA). The photoluminescence (PL) spectra of the resultant products were measured by a fluorescence spectrophotometer (FP-8600, JASCO, Japan) at room temperatures.

3. Results and discussions

Figure 1 shows particle morphologies for the three kinds of precursors. The rods exhibit uniform diameters in the range of ~80-150 nm, and lengths in the range of ~600-800 nm. The cubes were observed to have edge lengths in the range of ~1-1.5 μm. The 2D disk-like precursors (about ϕ 2 μm × 0.1 μm) exhibit uniform sizes. All the samples were found to be loosely aggregated with regular morphologies. The

structures of the three precursors were further determined by TEM observation combined with selected area electron diffraction (SAED) analysis, as shown in Figure 1 (d-f). All the three precursors diffracted as monocrystallines.

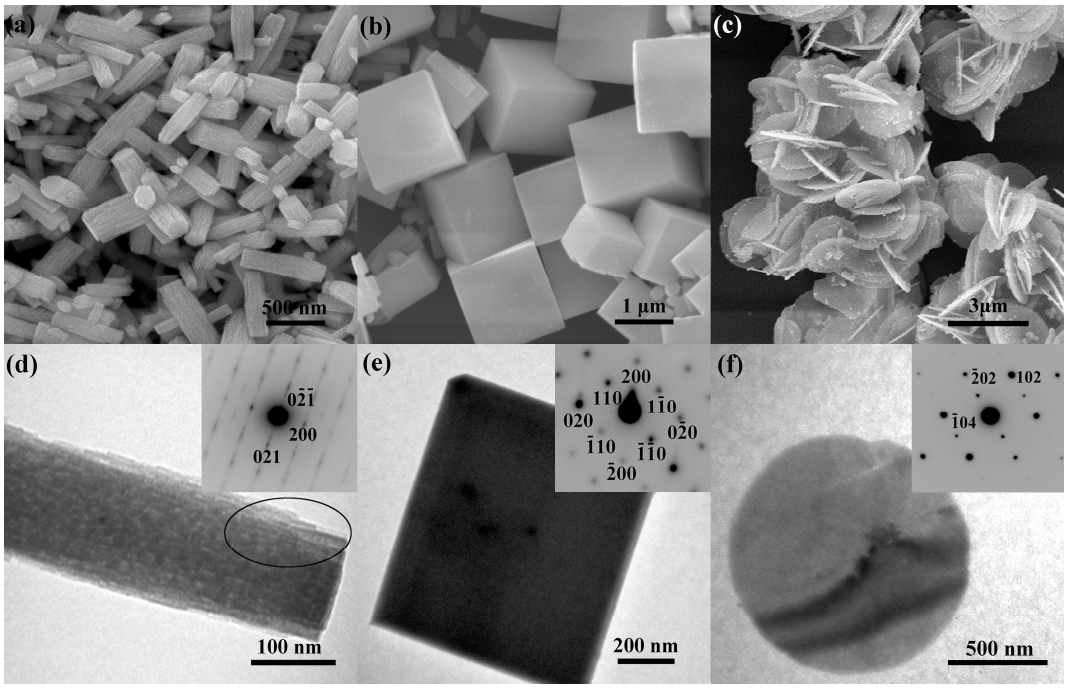

Fig. 1 FE-SEM images of the three typical precursors: (a) 1D rods (S1), (b) 3D cubes (S2), and (c) 2D disks (S3); TEM images of these precursors (d-f), and the insets show the corresponding SAED patterns.

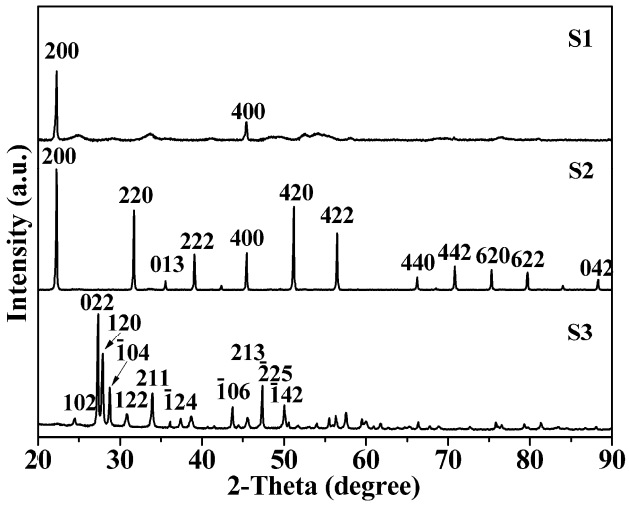

Fig.2 XRD patterns of the three typical precursors.

XRD analysis (Figure 2) shows that the rod-like precursor (S1) can be indexed to be cubic phase $In(OH)_3$ (lattice constant a = 7.979 Å, JCPDS card no. 73-1810) with {100} planes possessing strong and sharp diffraction intensity, suggesting that <200> maybe the dominant growth direction for one-dimension crystal.[28] Selected area electron diffraction (SAED) technique was used to verify this deduction, as described later. The diffraction peaks of the cubes (S2) can be indexed as cubic phase $In(OH)_3$. While, the disks (S3) can be indexed to be monoclinic phase $InOHSO_4(H_2O)_2$ (lattice constant a = 6.058 Å, JCPDS card no. 14-0608).

Table 1 summarizes the synthesis parameters adopted in this work. A general observation is that the structure and morphologies of the precursors are closely related to the crystallization environment. The composition of the precursors can be classified into two categories: $In(OH)_3$ and $InOHSO_4(H_2O)_2$.

1. Structure and morphologies of the $In(OH)_3$ precursors

The FT-IR spectra of samples S1 and S2 are displayed to indicate their surface states in Figure 3. The wide-adsorption bands in the region ~3500-3000 cm^{-1} and the weak absorption at 1627 cm^{-1}, providing evidence of adsorbed water, are assignable to the O-H and H-O-H, respectively.[29] The In^{3+}-O vibrations was detected with a strong peak at ~500 cm^{-1}.[30] The formation of In^{3+}-O band indicates that the oxygen atom is fixed to the In^{3+} ion, leaving the hydrogen free to vibrate about the oxygen atom in a bending mode, with the frequency occurring in the region ~1200-600 cm^{-1} (four splits).[30]

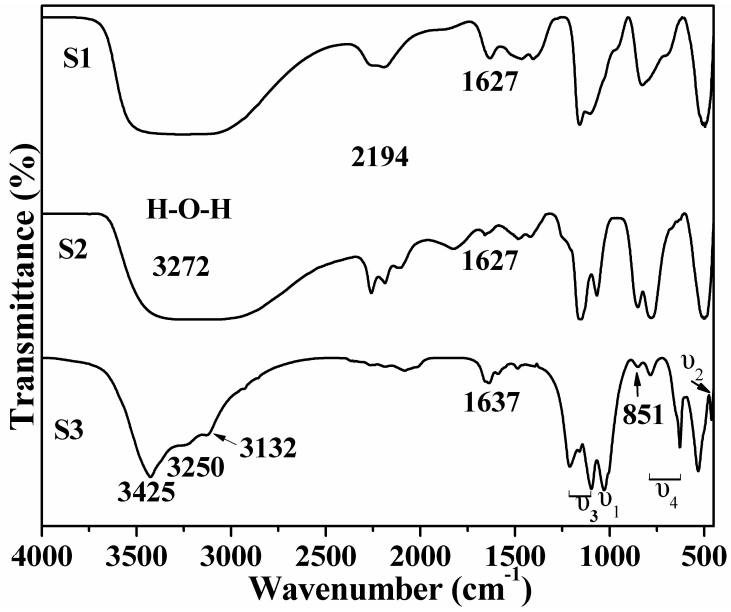

Fig. 3 FT-IR spectra for the three typical precursors.

As shown in Figure 1 (d, e), the two precursors both diffracted as the same crystalline phase, but presented different anisotropic growth, as a consequence of the effect of urea. It is well accepted that the external shape of a crystal is much determined by the relative development of various crystallographic faces, which governs their growth kinetics. Morphology evolution of the precipitates with time is shown in Figure 4. In the early stage (10 min), secondary particles were formed by the aggregation of small primary particles (about 20~30 nm). With the increase of reaction time, the particles gradually changed into rod-like, and grew in the axial direction, while the radius was almost invariant. It is clear that each individual rod was formed by the self-assembly of large amounts of primary particles. In the cubic phase $In(OH)_3$, the In atom is octahedrally surrounded by six oxygen atoms. The InO_6 octahedron is linked each other by corners along <100> and forms a 3D net-frame.[31] The crystalline $In(OH)_3$ is favor to grow and expose {100} under unconstrained conditions. It was found that urea, as a Lewis base, can coordinate to the $In(OH)_3$

crystals on (012), lowering the surface energy and inhibiting the growth along <012>. For the oriented attachment put forward by Banfiled et al.[32-34], the small single crystals are attached and rearranged to reduce the overall surface energy through sharing thermodynamically unstable crystal planes (perpendicular to (012)), and the interface elimination finally results in the formation of a bigger crystal. The elongated strips in the SEAD pattern (inset of Figure 1 (d)) should be attributed to the existence of layered structure parallel to the axial direction of the rods, [28] which also demonstrates the oriented attachment mechanism (OA). When a particle is attached on the surface of a rod, a small misorientation may be generated at the interface, forming the layered structure of the rod.

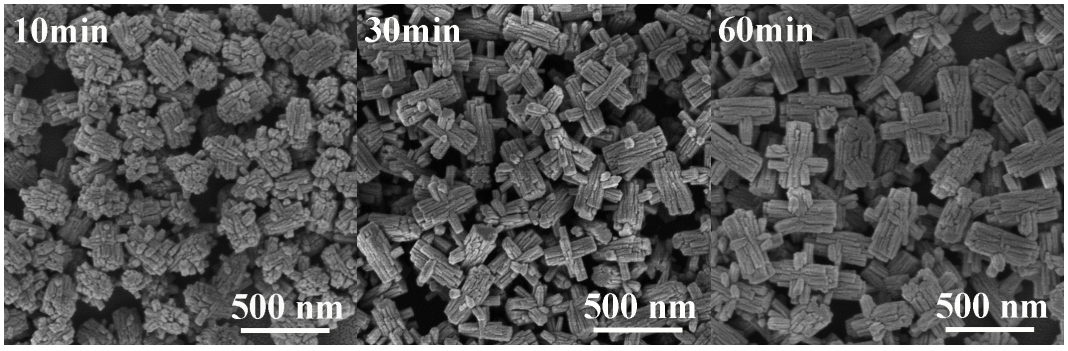

Fig. 4 Variation of morphology of the S1 particles with time after the first sight of turbidity from the clear solution.

When the original urea concentration is dropped to 0.06 M, cubic structured $In(OH)_3$ crystals tend to grow into cubic morphologies (S2), as shown in Figure 1(b). The $In(OH)_3$ particles tend to expose {100} planes, as shown in Figure 1(e). Morphology evolution of the colloidal particles with time after the appearance of visible turbidity in the originally transparent solution is shown in Figure 5. With the increase of time, the quantity of small particles decreases, and that of the big cubic

crystals increases, indicative of an Ostwald ripening process (OR).[35] Even though a few rods formed in the early stage, further growth of the cubes was dominant by assimilating the small particles.

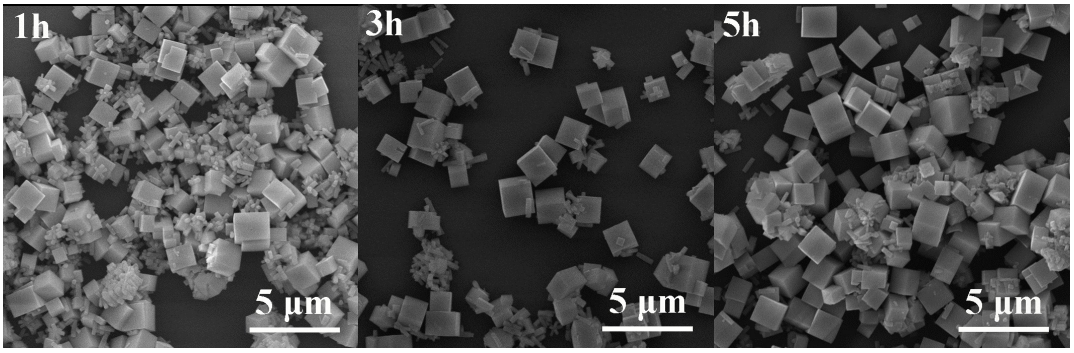

Fig. 5 Variations of morphology of the S2 particles with time after the first sight of turbidity from the clear solution.

2. Structure and morphologies of the monoclinic phase $InOHSO_4(H_2O)_2$ precursors

The functional groups built in the 2D disk-like precursors were investigated via FT-IR spectroscopy, as shown in Figure 3. The sharp absorption at ~3425 cm^{-1} is assignable to the stretching modes of free hydroxyl groups.[29] The broad bands with two peaks around 3250 and 3132 cm^{-1} and a peak at 1637 cm^{-1} are attributable to the three normal modes (the symmetric, asymmetric stretches and the bending vibration, respectively) of O-H vibration in water.[29] The observed two stretches (not apparent as a single broad absorption band), attributing to less chance of hydrogen bonding effects, imply that this sample contain water of hydration.[30] The fundamental IR vibrations of SO_4^{2-} are well documented to be located at 1104 cm^{-1} (ν_3), 981 cm^{-1} (ν_1), 618 cm^{-1} (ν_4) and 451 cm^{-1} (ν_2).[31] When the SO_4^{2-} tetrahedrons is distorted, ν_3 would split to give rise to two or three peaks, and ν_1 would become active usually near 1000 cm^{-1}. Similarly, the ν_4 absorption may split into three bands.[36] The appearance of ν1

vibration at ~1031 cm^{-1}, which is IR inactive in free SO_4^{2-} ions of highly symmetric in point group, together with the significant splitting of both ν_3 and ν_4, strongly suggest the presence of coordinated sulfate anions and also a possible intra-molecular coupling between SO_4^{2-} and OH^-.[36] The peak at ~536 cm^{-1} may be caused by the vibration of In^{3+}-O band.[30] The above results suggest that the S3 precursor is a hydration basic sulfate, in accordance with the results of XRD in Figure 2.

The $InOHSO_4(H_2O)_2$ precursors grew into round disks with a diameter of about 2 μm, as shown in Figure 1(c). The SAED pattern of the precursor (Figure 1(f)) indicates that the disks are of single crystalline. The facets parallel to the disk surface was indexed to be (010). The morphology evolution of the precipitate with time is shown in Figure 6. It can be seen that the disks grew in the radius direction, while the thickness was almost invariant. It is well documented that each indium atom in the compound $InOHSO_4(H_2O)_2$ is octahedrally surrounded by six oxygen atoms, and the InO_6 polyhedrons are joined together by common corners, forming periodic bond chains running parallel to the b axis.[37] Each parallel chain is then connected to other identical chains by hydrogen bonds, as shown in Scheme 1. It was considered that the prolonged growth of chains may be inhibited by the coordination between InO_6 polyhedrons and the excessive SO_4^{2-} ion.[38] According to the basic theory of periodic bond chain (PBC) and attachment energy (AE) considerations,[39,40] the facets parallel to (010) of the disk could be considered as the flat (F) faces. The new born crystal can easily be bound by the straight edges that are parallel to the Kink faces (perpendicular to b axial), in which the growth units are bonds by uninterrupted chains of strong

bonds or periodic bond chains. The screw-like ladders, found on the disk-like precursors (S3), give evidence for this conjecture, as shown in the inset of Figure 6. The crystal tends to homogenize the growth rates on the a-c plane (010) perpendicular to the b axis, resulting in the disk-like morphology instead of the hexagonal plate in the early stage. The longer the reaction time, the lower the concentration of urea in the reaction system, and the lower the isotropic interfacial energy.[41] Thus, the crystalline grew into hexagonal plates instead of round disks when the reaction time reached to 120 min. To confirm the effects of urea, ceteris paribus, a comparative experiment was carried out where the urea concentration was 0.06 M compared to that of 9 M for sample S3. Even though fragmentation of some of the particles can be observed, the particles mainly grew into hexagonal plates, as shown in Figure S3.

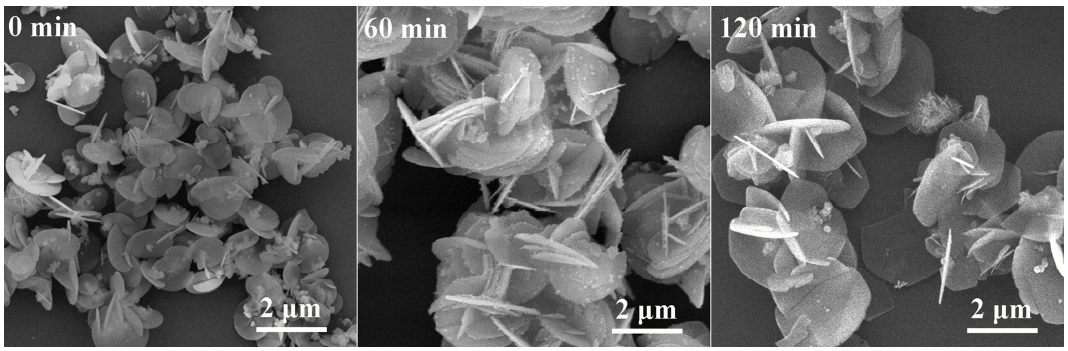

Fig. 6 Variation of morphology of the S3 particles with time after the first sight of turbidity from the clear solution.

3. The effect of urea and K_2SO_4 on composition and morphology of the precursors

Based on the above analysis, the composition and morphologies of In-complex precursor is highly affected by the concentration of urea and K_2SO_4. The crystalline growth is controlled by the mechanisms as shown in Scheme 1.

For specimen S1, the urea concentration is high, and large amounts of OH^- ions can be produced at the reaction temperature. The hydrolysis of urea in aqueous solution can be expressed as:

$$NH_2(CO)NH_2 + 3H_2O \rightarrow 2NH_4^+ + 2OH^- + CO_2 \uparrow \quad (1)$$

The OH^- ions formed react with In^{3+} ions or indium complex in the solution to form precursors:

$$In^{3+} + 3OH^- \rightarrow In(OH)_3 + 3Cl^- \quad (2).$$

According to the LaMer theory[42], the large amounts of OH^- released can result in the explosive nucleation of small particles. At the same time, urea can also alter the crystalline habit of the precursors by inhibiting the growth of crystal on certain site. It was found that urea can selectively coordinated or absorbed on the {012} of $In(OH)_3$. The primary particles then oriented self-assembled onto the rod-like secondary particles, the side surface of which appears as many {012} of small primary particles for reducing the overall surface energy. In contrast, for precursor S2, {100} were exposed due to the weak preferential adsorption of urea, since the initial urea concentration is low.

It has been proven that indium exists as sulfate complex in aqueous indium sulphate solutions.[24,38] For precursor S3, the composition of the precursor is tunable by the addition of K_2SO_4. The formation of $InOHSO_4(H_2O)_2$ can be expressed as:

$$In^{3+} + OH^- + SO_4^{2-} + 2H_2O \rightarrow InOHSO_4(H_2O)_2 \quad (2)$$

The addition of K_2SO_4 facilitates the formation of In-sulfate complex, which in turn reduces the local concentration of In^{3+} ions available for the reaction with OH^-.

Thus, the nucleation rate was substantially reduced by the addition of K_2SO_4, and single crystals with micrometer size were formed.

The $InOHSO_4(H_2O)_2$ crystal grows mainly in the direction perpendicular to b axis. In the radial direction, each InO_6 polyhedrons chain is connected to six neighboring chains by hydrogen bond, as shown in Scheme 1. It can be imagined that the precursor prefers to show hexagonal plates under unconstrained conditions. Based on the Langmuir adsorption model developed by Amjad and Maniatis[30], urea can rapidly absorbed at the active growth sites, e.g., at the edge angle of the crystal. The higher the urea concentration was, the more the isotropic interfacial energy generated, and the smoother the edge of the disk grew.

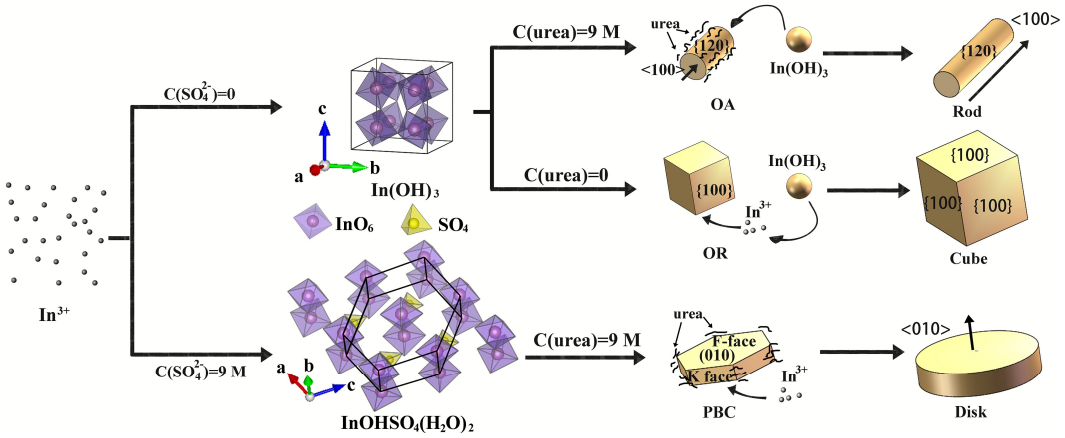

Scheme 1. Schematic illustration showing the formation mechanism of the In-complex precursors with various morphologies. The crystal structure of $In(OH)_3$ and $InOHSO_4(H_2O)_2$ were visualized by Visualization for Electronic and Structural Analysis (VESTA) 3[43].

4. Thermal behavior and phase evolution of the precursors

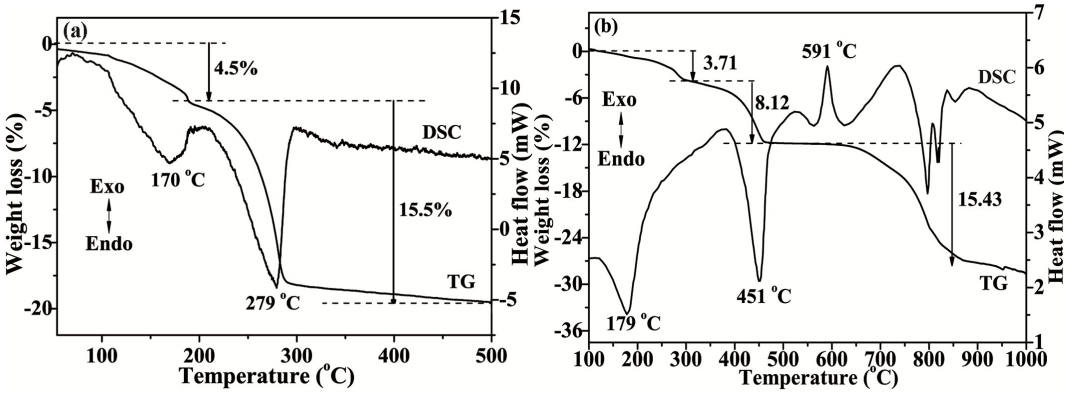

Fig. 7 DSC-TG curves for (a) the $In(OH)_3$ precursor (S1), and (b) the $InOHSO_4(H_2O)_2$ precursors (S3) at a heating rate of 10 °C/ min in oxygen.

Figure 7 (a) shows thermal analysis of the rod-like precursor (S1) recorded in flowing oxygen at a heating rate of 10 °C/ min. The cube-like precursor (S2) exhibits a similar thermal behavior and thus the data are not shown. The thermal behavior observed herein is typical of $In(OH)_3$, as reported by Yan et al.[44], and it was shown that this compound decomposes to In_2O_3 at a temperature of about 300 °C. After calcining at 600 °C for 1 h, both precursors displayed the characteristic diffractions corresponding to the cubic structured In_2O_3 phase, as shown in Figure S1. The decomposition process can be described as follows.

$$In(OH)_3 \rightarrow In_2O_3 + H_2O \quad (4)$$

For precursor S3, a three-step weight loss was observed in the TG curve (Figure 7 (b)). The first step weight loss (about 3.71%), accompanied by an endothermic peak, is primarily caused by the evaporation of absorbed water. The second step weight loss (about 8.12%), corresponding to the large endothermic at 450 °C, is due to the decomposition of $InOHSO_4(H_2O)_2$, as shown by Equation 5.

$$4In(OH)SO_4(H_2O)_2 \rightarrow 2InH(SO_4)_2 \cdot H_2O + In_2O_3 + 7H_2O \quad (5)$$

The plateau region in the TG curve from 450 ^{o}C to 650 ^{o}C, with a sharp exothermal peak at 591 ^{o}C, indicates the crystallization of orthorhombic $InH(SO_4)_2 \cdot H_2O$. The third step weight loss, accompanied by a series of endothermic peaks, corresponds to the loss of sulfate and crystal water, obtaining In_2O_3.

$$2InH(SO_4)_2 \cdot H_2O \rightarrow 4SO_2 + 2O_2 + 3H_2O + In_2O_3 \quad (6)$$

The thermal decomposition and phase evolution process was further confirmed by the XRD patterns of the as-synthesized and calcined powders of sample S3 at various temperatures, as shown in Figure S2. After calcining at 900 ^{o}C for 1 h, the products displayed the characteristic diffractions corresponding to the cubic structured In_2O_3 phase.

5. Morphology and photoluminescence behavior of the In_2O_3 particles

The morphologies of the In_2O_3 almost inherited the initial morphologies of the precursors, except for a little cracking for the internal stress created in the calcination process, as shown in Figure 8.

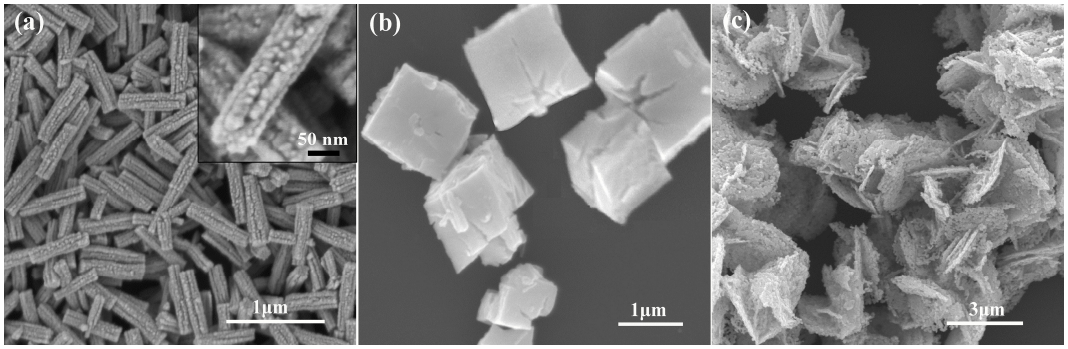

Fig. 8 FE-SEM images showing the three kinds of In_2O_3 post annealed from different precursors: (a) 1D rods (S1), (b) 3D cubes (S2), and (c) 2D disks. The inset in part (a) is the magnified image of an individual rod.

The photoluminescence properties of the post annealing-produced In_2O_3 samples

were investigated and shown in Figure 9. It is shown that all of the In_2O_3 particles show a strong PL emission in the green spectral region under blue light excitation. Figure 9 (a) compares the PL spectra of the In_2O_3 converted from S1, S2 and S3, respectively, and all of them were annealed at 400 ^oC for 1h in air. Irrespective of particle morphology, both of the PL and PLE bands appeared at essentially identical positions. The excitation spectrum consists of multiple peaks with a maximum at 444 nm (2.8 eV), due to the band-gap excitation of the In_2O_3 semiconductor.[45] Upon excitation into the band gap of In_2O_3 at 444 nm, the obtained PL spectrum exhibits a broad band from 500 to 540 nm with a maximum at 506 nm. As a typical n-type semiconductor, cubic In_2O_3 has an oxygen-deficient fluorite structure, which would induce the formation of new energy levels in the band gap.[46] The green emission from the as-prepared In_2O_3 particles should thus be resulted from the recombination of an electron occupying oxygen vacancies with a photoexcited hole, as illustrated in Figure 9 (b). Under the excitation of 444 nm, the electrons are excited from the valence band (VB) to the conduction band (CB). The electrons move freely in the CB and finally relax to the oxygen vacancies. The recombination of an electron occupying oxygen vacancy with a photoexcited hole yields the green emission with the wavelength in the range 500~540 nm. The intensity of the PLE and PL bands differed significantly among the three samples and increased in the order rods < cubes < disks. The effect of morphologies on luminous intensity is originated from specific surface area and the aggregation of primary particles. A higher specific surface area corresponds to a larger quantity of oxygen vacancies,[47] leading to a stronger luminous intensity. As a result,

the disk-like sample (specific surface area: 8.59 m^2/g) shows a stronger luminous intensity than that of the cubes (specific surface area: 3.20 m^2/g). On the other hand, the scattering of the incident light is facilitated for the rods particles which consist of self-assembly of many small In_2O_3 nanoparticles (specific surface area: 33.51 m^2/g), leading to the weakest luminescence.[48]

To further understand the effect of oxygen deficiencies on emissions from In_2O_3, the In_2O_3 samples were re-annealed in O_2 at 400 ^oC, and the emission evolution was detected, as shown in Figure 9 (c). It was observed that the luminous intensity decreases with increasing annealing time. For the 506 nm emission, the relationship between emission intensity and annealing time was fitted using the following equation:

$$I = A\exp(-t/\tau) + B \quad (7)$$

where I and t are emission intensity and annealing time, respectively. τ can be considered as the 'effective' annealing relaxation time of emission intensity. A and B are constants. The fittings yielded: τ = 7.65 min, A = 72.91 (au) and B = 806.55 (au) for sample S1 (rods); τ = 11.84 min, A = 105.30 (au) and B = 832.64 (au) for sample S2 (cubes); and τ = 8.19 min, A = 38.30 (au) and B = 1006.79 (au) for sample S3 (disks). The three oxides have specific surface area in the order: rods (33.51 m^2/g) > disk (8.59 m^2/g) > cubes (3.20 m^2/g). Clearly, the larger the specific surface area is, the shorter the relaxation time become. For In_2O_3 particles with higher specific surface area, the oxygen deficiencies can be eliminated more quickly duo to the more ambient molecular O_2 to strike the unoccupied oxygen site. [49] It is thus further certify

that the green emissions are largely attributed to oxygen deficiencies in In_2O_3, and can be weakened by eliminating oxygen deficiencies. The three samples were then experience third time annealing in air at 400 ^oC for 30 min, and the luminous intensities of all three samples were detected to recover, as shown in Figure 9 (d). The result reveals that the luminous intensity is dependence on the atmosphere in annealing. The luminous intensity can be enhanced for sample annealed in air compared to that annealed in O_2.

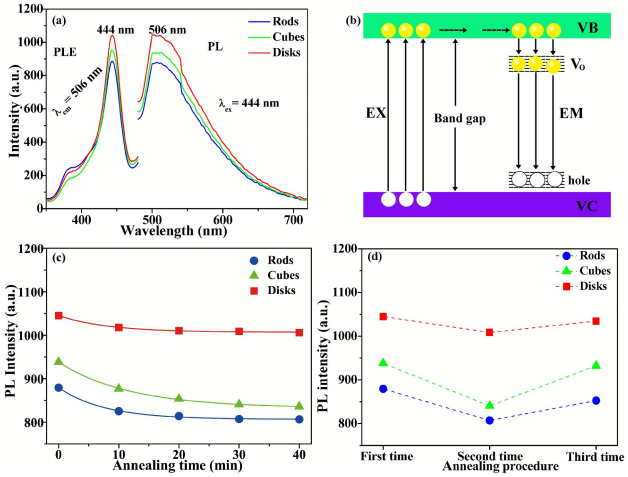

Fig. 9 (a) PLE and PL spectra (λ_{ex}=444 nm) of the In_2O_3 with different morphologies annealed in air at 400 ^oC for 1 h; (b) the simple schematic model illustrating the excitation and emission process for In_2O_3; (c) the evolution of 506 nm emission intensity of the three samples as a function of annealing time in O_2 at 400 ^oC; and (d) the 506 nm emission intensity of the three In_2O_3 samples in three times annealing at 400 ^oC, in which the first time is in air for 1h, the second time is in O_2 for 40 min and the third time is in air for 30 min.

4. Conclusion

In summary, In_2O_3 powders with three distinctive morphologies of rods (about ϕ

0.1 μm × 0.8 μm), cubes (about 1.5 μm × 1.5 μm × 1.5 μm), and disks (about φ 2 μm × 0.05 μm) have been synthesized via a facile urea-based homogeneous precipitation method.

In the absence of K_2SO_4, $In(OH)_3$ precursors were synthesized. Urea concentration was found to have significant effect on morphology of the precursor particles. With a comparatively high urea concentration, the mesocrystalline rod-like $In(OH)_3$ precursor was produced, with <100> parallel to the axial direction. Each $In(OH)_3$ rod is composed of the aggregation of large amounts of oriented small $In(OH)_3$ particles. The formation mechanism was thought to be coordination of urea on {012} of the primary particles, which results in the orientated attachment of the small crystals on the end of the rod, with <100> parallel to the axial direction. With a comparatively low urea concentration, the coordination effect of urea is weak, and cube-like $In(OH)_3$ crystals were obtained by Ostwald ripening with exposed {100}. The addition of K_2SO_4 was found to affect the morphology and composition of the precursor, resulting in the formation of $InOHSO_4(H_2O)_2$ disks. The addition of K_2SO_4 facilitates the formation of In-sulfate complex, lowers the nucleation rate, and results in the $InOHSO_4(H_2O)_2$ disk with about 2 μm in diameter. The disk growth follows the PBC mechanism and AE consideration, with b axis of the lattice perpendicular to the disc surface. Upon blue light excitation, the three types of In_2O_3 showed a green emission owing to oxygen vacancy. The luminous intensity of In_2O_3 increases in the order: rods < cubes < disks. The intensity can be reduced by annealing in O_2 to eliminate the amount of oxygen vacancy, and inversely enhanced by annealing in air.

5. Acknowledgement

This work is supported by the Joint Funds of the National Natural Science Foundation of China (U1302272), the Fundamental Research Funds for the Central Universities (grants N141006002), and the fund of the State Key Laboratory of Advanced Technologies for Comprehensive Utilization of Platinum Metals (SKM-SPM-201206, SKL-SPM-201214, SKL-SPM-201505 and SKL-SPM-201506).

6. Reference

1. Y. D. Shen, S. Turner, P. Yang, G. V. Tendeloo, O. I. Lebedev, and T. Wu, *Nano Lett.*, 2014, 14, 4342-4351.
2. C. H. Choi, S. Y. Han, Y. W. Su, Z. Fang, L. Y. Lin, C. C. Cheng, and C. H. Chang, *J. Mater. Chem. C*, 2015, 3, 854-860.
3. F. C. Lei, Y. F. Sun, K. T. Liu, S. Gao, L. Liang, B. C. Pan, and Y. Xie, *J. Am. Chem. Soc.*, 2014, 136, 6826-6829.
4. K. Hwang, Y. S. Jung, Y. J. Heo, F. H. Scholes, S. E. Watkins, J. Subbiah, D. J. Jones, D. Y. Kim, D. Vak, *Adv. Mater.*, 2015, 27, 1241-1247.
5. J. E. Ellis, U. Green, D. C. Sorescu, Y. Zhao, and A. Star, *J. Phys. Chem. Lett.*, 2015, 6, 712-717.
6. V. S. Vaishnav, S. G. Patel and J. N, Panchal, *Sonsor. Actuat. B -Chem.*, 2014, 202, 1002-1009.
7. V. S. Vaishnav, S. G. Patel and J. N, Panchal, *Sonsor. Actuat. B -Chem.*, 2015, 206, 381-388.
8. Y. D. Shen, S. Turner, P. Yang, G. Van Tendeloo, O. I. Lebedev and T. Wu, *Nano Lett.*, 2014, 14, 4342-4351.
9. K. Yadav, B. R. Mehta and J. P. Singh, *Appl. Surf. Sci.*, 2015, 346, 361-365

10. Z. M. Li, P. Y. Zhang, J. G. Li, T. Shao, J. Wang and L. Jin, *Catal. Commun.*, 2014, 43, 42-46.
11. X. H. Mu, C. L. Chen, L. Y. Han, B. Q. Shao, Y. L. Wei, Q. L. Liu and P. H. Zhu, *J. Alloy. Compd.*, 2015, 637, 55-61.
12. S. S. Ghosh, P. K. Biswas and S. Neogi, *Sol. Energy*, 2014, 109, 54-60.
13. V. V. Jadhav, D. V. Shinde, S. A. Patil, S. D. Liu, S. U. Mutkule, M. Naushad, R. S. Mane, K. N. Hui, and S. H. Han, *Scripta Mater.*, 2015, 107, 54-58.
14. R. Q. Li, L. L. Li, W. W. Zi, J. J. Zhang, L. Liu, L. C. Zou and S. C. Gan, *New J. Chem.*, 2015, 39, 115-121.
15. J. J. Liu, G. Chen, Y. G. Yu, Y. L. Wu, M. J. Zhou, W. Zhang, H. Qin, C. D. Lv and W. Fu, *New J. Chem*., 2015, 39, 1930.
16. J. J. Liu, G. Chen, Y. G. Yu, Y. L. Wu, M. J. Zhou, H. Q. Zhang, C. D. Lv, Y. Zhang and F. He, *RSC Adv.*, 2015, 5, 44306.
17. C. Ma, X. D. Li, S. H. Liu, Q. Zhu, D. Huo, J. G. Li and X. D. Sun, *Ceram. Int.*, 2015, 41, 9577-9584.
18. Z. Liu, K. Dong, J. H. Liu, X. L. Han, J. S. Ren and X. G. Qu, *Small*, 2014, 10, 2429-2438.
19. H. M. Qin, X. H. Zhang, H. Liu, Y. H. Sang and J. Y. Wang, *CrystEngComm*, 2013, 15, 5076-5081.
20. X. J. Xu, X. D. Sun, H. Liu, J. G. Li, X. D. Li, D. Huo, and S. H. Liu, *J. Am. Ceram. Soc.*, 2012, 95, 3821-3826.
21. Y. Ohhata, F. Shinoki and S. Yoshida, *Thin Solid Films*, 1979, 59, 255.
22. S. T. Jean and Y. C. Her, *Cryst. Growth Des.*, 2010, 10, 2104-2110.
23. G. X. Wang, J. S. Park, D. Wexler, M. S. Park and J. H. Ahn. *Inorg. Chem.*, 2007, 46, 4778-4780.

24. D. V. Shinde, D. Y. Ahn, V. V. Jadhav, D. Y. Lee, N. K. Shrestha, J. K. Lee, H. Y. Lee, R. S. Mane and S. H. Han, *J. Mater. Chem. A*, 2014, 2, 5490.
25. H. L. Wei, L. Zhang, Z. L. Liu, and K. L. Yao, *Chin. Phys. B*, 2011, 20, 118102.
26. O. Bierwagen, *Semicond. Sci. Techol.*, 2015, 30, 024001
27. E. A. Forsh, A. M. Abakumov, V. B. Zaytsev, E. A. Konstantinova, P. A. Forsh, M. N. Rumyantseva, A. M. Gaskov, and P. K. Kashkarov, *Thin Solid Films*, 2015, 595, 25-31
28. S. B. Sun, X. T. Chang, Z. J. Li, *Mater. Charact.*, 2012, 73, 130-136.
29. J. A. Gadsden, *Infrared Spectra of Minerals and Related Inorganic Compounds*, Butterworth, Newton, 1975.
30. H. Yang, L. Liu, H. Liang, J. Wei, Y. Yang, *CrystEngComm*, 2011, 13, 5011–5016
31. L Schlicker, R Riedel and A Gurlo, *Nanotechnology*, 2009, DOI: 10.1088/0957-4484/20/49/495702
32. R. L. Penn and J. F. Banfield, *Science*, 1998, 281, 969-971.
33. J. F. Banfield, S. A. Welch, H. Z. Zhang, T. T. Ebert and R. L. Penn, *Science*, 2000, 289, 751-754.
34. D. S. Li, M. H. Nielsen, J. R. I. Lee, C. Frandsen, J. F. Banfield and J. J. De Yoreo, *Science*, 2012, 336, 1014-1018.
35. M. Gong, W. Zhou, M. C. Tsai, J. G. Zhou, M. Y. Guan, M. C. Lin, B. Zhang, Y. F. Hu, D. Y. Wang, J. Yang, S. J. Penneycook, B. J. Hwang, and H. J. Dai, *Nat. Commun.*, 2014, 22, doi:10.1038/ncomms5695.
36. X. J. Wang, J. G. Li, Q. Zhu, X. D. Li, X D. Sun, and Y. Sakka, *Sci. Technol. Adv. Mater.*, 2014, 15, doi:10.1088/1468-6996/15/1/014204.
37. J. Majzlan, C. N. Alpers, C. B. Koch, R. B. McCleskey, S. C. B. Myneni, and J. M. Neil, *Chem. Geol.*, 2011, 284, 296-305.

38. W. W. Rudolph, D. Fischer, M. R. Tomney and C. C. Pyr, *Phys. Chem. Chem. Phys.*, 2004, 6, 5145-5155.

39. J. A. P. Sato, F. N. Costa, M. D. D. Rocha, E. J. Barreiro, C. A. M. Fraga, F. Punzo and R. F. Ferreira, *CrystEngComm*, 2015, 17, 165-173.

40. F. R. Massaro, M. Moret, M. Bruno and D. Aquilane, *Cryst. Growth Des.*, 2013, 13, 1334-1341.

41. L. Q. Wei, S. F. Ye, Y. J. Tian, Y. S. Xie, Y. F. Chen, *J. Cryst. Growth*, 2009, 311, 3359-3363.

42. V. K. LaMer, R. H. Dinegar, *J. Am. Chem. Soc.*, 1950, 72, 4847-4854.

43. K. Momma and F. Izumi, *J. Appl. Crystallogr.*, 2011, 44, 1272-1276.

44. T. J. Yan, W. J. Li, S. W. Bi and J. M. You, *J. Nanosci. Nantechno.*, 2015, 15, 2197-2203.

45. J. Yang, C. K. Lin, Z. L. Wang and J. Lin, *Inorg. Chem.*, 2006, 45, 8973-8979.

46. J. A. J. Pardoe, and A. J. Downs, *Chem. Rev.*, 2007, 107, 2-45

47. Y. Zhao, J. Liu, L. Y. Shi, S. Yuan, J. H. Fang, Z. Y. Wang, and M. H. Zhang, *Appl. Catal. B -Environ.*, 2010, 100, 68-76.

48. Q. Zhu, J. G. Li, X. D. L and X. D. Sun, *Acta Mater.*, 2009, 57, 5975-5985.

49. X. D. Zhu, W. D. Si, X. X. Xi, and Q. D. Jiang, *Appl. Phys. Lett.*, 2001, 78, 460-462.

Graphical Table of Contents

Synthesis and formation mechanism of morphology-controllable indium containing precursors and optical properties of the derived In_2O_3 particles

Zhijie Lin,Qi Zhu, Yu Dong, Shaohong Liu, Ji-Guang Li*, Xiaodong Li, Di Huo, Mu Zhang, Ming Xie, Xudong Sun*

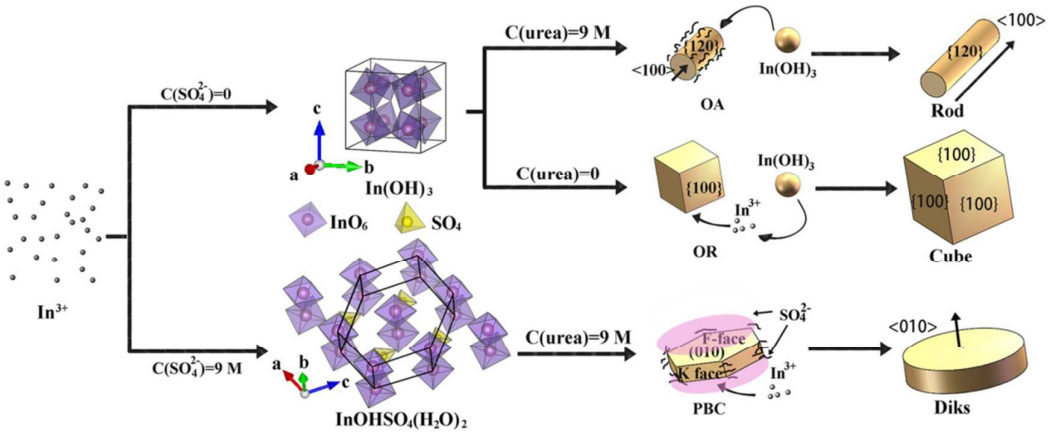

Indium containing precursors with three morphologies were synthesized, and the formation mechanisms were analyzed.